Guest Inclusion Modulates Concentration and Persistence of Photogenerated Radicals in Assembled Triphenylamine Macrocycles

Ammon J. Sindt,[†] Baillie A. DeHaven,[†,⊥] Dustin W. Goodlett,[†] Johannes O. Hartel,[†] Pooja J. Ayare,[†] Yong Du,[‡] Mark D. Smith,[†] Anil K. Mehta,[§] Alexander M. Brugh,[∥] Malcolm D. E. Forbes,[∥] Clifford R. Bowers,[‡] Aaron K. Vannucci,[†] and Linda S. Shimizu*,[†]

[†]Department of Chemistry and Biochemistry, University of South Carolina, Columbia, South Carolina 29208, United States

[‡]Department of Chemistry, University of Florida, Gainesville, Florida 32611, United States

[§]National High Magnetic Field Laboratory and McKnight Brain Institute, University of Florida, Gainesville, Florida 32610, United States

[∥]Department of Chemistry and Center for Photochemical Sciences, Bowling Green State University, Bowling Green, Ohio 43403, United States

Ⓢ *Supporting Information*

ABSTRACT: Substituted triphenylamine (TPA) radical cations show great potential as oxidants and as spin-containing units in polymer magnets. Their properties can be further tuned by supramolecular assembly. Here, we examine how the properties of photogenerated radical cations, intrinsic to TPA macrocycles, are altered upon their self-assembly into one-dimensional columns. These macrocycles consist of two TPAs and two methylene ureas, which drive the assembly into porous organic materials. Advantageously, upon activation the crystals can undergo guest exchange in a single-crystal-to-single-crystal transformation generating a series of isoskeletal host−guest complexes whose properties can be directly compared. Photoinduced electron transfer, initiated using 365 nm light-emitting diodes, affords radicals at room temperature as observed by electron paramagnetic resonance (EPR) spectroscopy. The line shape of the EPR spectra and the quantity of radicals can be modulated by both polarity and heavy atom inclusion of the encapsulated guest. These

Persistent & Regenerable Radicals

photogenerated radicals are persistent, with half-lives between 1 and 7 d and display no degradation upon radical decay. Re-irradiation of the samples can restore the radical concentration back to a similar maximum concentration, a feature that is reproducible over several cycles. EPR simulations of a representative spectrum indicate two species, one containing two N hyperfine interactions and an additional broad signal with no resolvable hyperfine interaction. Intriguingly, TPA analogues without bromine substitution also exhibit similar quantities of photogenerated radicals, suggesting that supramolecular strategies can enable more flexibility in stable TPA radical structures. These studies will help guide the development of new photoactive materials.

INTRODUCTION

Construction of hierarchical materials through supramolecular assembly of small molecules is an expedient method for crafting materials with useful properties.[1−4] These properties range from conductivity[5] and magnetism[6] to dichroism.[7] In addition, supramolecular assembly can also be used to make porous materials that encapsulate small guests.[8,9] This leads to materials of use in catalysis,[10,11] storage,[12,13] confinement,[14] separation,[15,16] and sensing.[17,18] Furthermore, bound guests may alter the chemical and physical properties of the host itself, for example, modulating the rotational speed of host-bound molecular rotors[19] or expanding/contracting the host framework.[20,21] Here, we investigate how different guests encapsulated within a triphenylamine (TPA) host affect its ability to form radicals in the solid state upon UV irradiation (Figure 1). The host is robust and exchanges guests via single-crystal-to-single-crystal (SC-SC) transformations while retaining its original framework. This affords a series of isoskeletal

host−guest structures whose properties can be directly compared. Upon UV irradiation of the host, long-lived radicals are generated. Encapsulated guests within the host modulate the line shape of their electron paramagnetic resonance (EPR) spectra and the concentration of radicals observed during irradiation. Additionally, after decay of the photogenerated radicals, samples can be re-irradiated to regenerate the observed radicals without harming or degrading the TPA host. Understanding how guest inclusion affects these radical properties will be useful for designing the next generation of conductive and magnetic materials.

Organic radicals have many uses, ranging from magnetic resonance imaging (MRI) contrasting agents[22] to multifunctional magnetic materials.[23] One class of these radicals is TPA radical cations, which have undergone a single electron
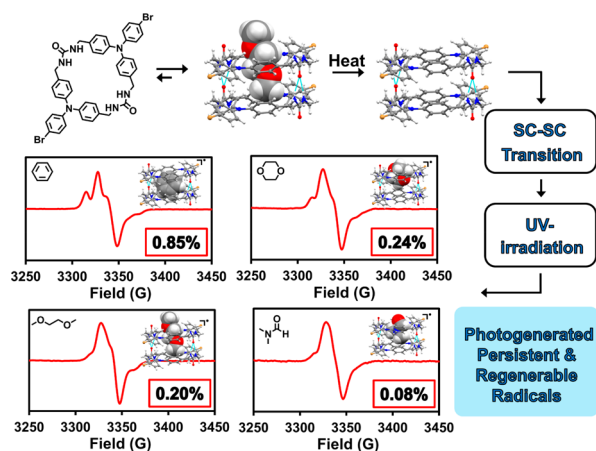
Figure 1. Self-assembly of TPA macrocycles results in the formation of a columnar assembled host. Activation of this host by heating allows for the introduction of new guests via SC-SC transformations. Each complex generates radicals upon irradiation with 365 nm LEDs, affording EPR spectra with different line shapes and intensities. A comparison of four of these EPR is shown above (benzene, 1,4-dioxane, DME, and DMF). The insets for each graph show structure of the guest, SC-XRD of the host–guest complex, and the percent of molecules that generate a radical upon UV-irradiation at the maximum radical concentration compared to the total number of molecules in the bulk material.

Figure 2. Comparison of TPA structures investigated. Macrocycles **1** and **1a**, linear analogues **2** and **2a**, and control compounds **3**, **3a**, and **4** are shown.

oxidation from their neutral state.[24] Key to their stability is the presence of *para* substitution on all three phenyl rings of the TPA system, which slows degradation reactions such as benzidine formation.[25,26] This is seen for Magic Blue, a commercial one-electron oxidant,[27,28] as it has bromine substitution on all three *para* sites of the TPA. When stabilized, TPAs find use as high-spin polymers,[29,30] cathodes in batteries,[31,32] and as hole-transport layers in solar cells.[33] Typically, these radicals are formed through chemical or electrochemical oxidation pathways,[34] but they may also be generated by UV irradiation when an electron acceptor is present.[35,36]

Our group employs the three-centered urea hydrogen-bonding interaction to organize linear and macrocyclic compounds in high fidelity. This affords nanoporous materials that are typically used as nanoreactors for photochemical reactions.[37] In addition to forming nanochambers, these structures also exhibit markedly different photophysical properties when compared to their unassembled monomers in solution. For example, assembly of benzophenone-containing urea macrocycles and linear analogues display surprisingly stable radical formation upon UV irradiation; this behavior is not observed in solution.[38] Similarly, brominated TPA **2a** (Figure 2) also shows enhanced stability of photogenerated radicals within its assembled structure, while radical formation in solution results in complete degradation of the TPAs,[39] thus demonstrating the importance of supra-molecular assembly on the overall stability of the photo-generated radicals. Here, we investigate if TPA-containing macrocycle system **1a** also exhibits enhanced photogenerated radical stability upon self-assembly.

TPA **1a** self-assembles to form a porous host that can facilitate guest inclusion and removal via SC-SC crystal transformations.[40] By irradiating this host we can probe if macrocycle **1a** exhibits similar radical formation as its linear analogue counterpart **2a** and if guest inclusion alters the
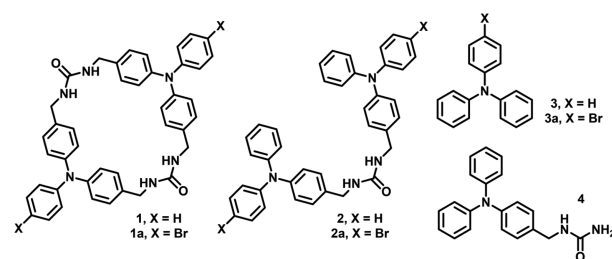
process of radical generation within the host. Thus, the photophysical properties and photogenerated radical formation of this host were investigated. The guests in these studies were selected to cover a range of polarities as well as heavy atom inclusion. Control compounds **1**, **2**, and **3**–**4** were prepared to elucidate the structure of the photogenerated radicals and to identify the features of these assembled TPA systems that allow for stable radical formation. Our goal is to understand the effects different guests have on radical formation and to determine what characteristics are necessary for TPA-containing compounds to exhibit these properties.

■ RESULTS AND DISCUSSION

Macrocycles (**1** and **1a**) and linear analogues (**2** and **2a**) were synthesized in five steps following established methods (Scheme S1).[39,40] For macrocycle **1**, its dibromide and protected macrocycle precursor were structurally characterized (see Supporting Information). Control compounds **3** and **3a** were purchased from commercial suppliers, while control **4** was synthesized in two steps using a Vilsmeier–Haack reaction to yield the aldehyde,[41] followed by a reductive alkylation of urea to give the desired product.[42] Host–Guest crystals of **1** and **1a** were obtained from vapor diffusion of either water or 1,2-dimethoxyethane (DME), respectively, into dimethyl sulfoxide (DMSO) solutions. Solvent-free crystals for **2**–**4** were grown via slow evaporation of acetonitrile (**2** and **3a**), ethyl acetate (**2a**), or ethanol (**3**) or by vapor diffusion of water into a dimethylformamide (DMF) solution (**4**).

For TPA **1**, the X-ray structure revealed the desired macrocycle in the space group $P2_1/n$ of the monoclinic system. The macrocycles were found in the *syn* conformation organized into tubular columns encapsulating disordered DMSO in a 1:1 host–guest ratio. The *syn* conformation was surprising, as previous *bis*-urea macrocycles crystallized in the *anti*-conformation, where the urea groups in a single macrocycle were oppositely aligned to minimize dipole interactions.[37] Despite this, the macrocycles still organize into columns through the characteristic three-centered urea hydrogen bond ($d(N\cdots O) = 3.090(5)$, $3.078(5)$, $3.147(5)$, and $3.063(5)$ Å). Additional stabilization occurs through intra-columnar edge-to-face π-stacking of the TPA groups (Figure S22). This stacking affords individual nanotubes with a pore aperture of 6.4×4.3 Å after accounting for the van der Waals (vdW) radii of the participating atoms (Figure 3A, top). The resulting nanotubes pack together to form robust hexagonal arrays as seen in Figure S16.

For comparison, the brominated macrocycle **1a** crystallizes as colorless needles in the space group $P2_1/c$ of the monoclinic system.[40] This macrocycle adopts the typical *anti* conformation and organizes into columnar tubes. The channels display an
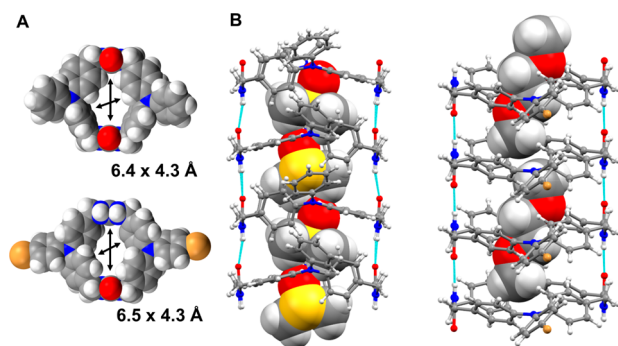
Figure 3. Comparison of TPA hosts **1**·DMSO and **1a**·DME. (A) Comparison of cross-sectional areas with **1** on top and **1a** on bottom (subtracting vdW radii). (B) Comparison of columnar structures with guests included with **1**·DMSO on the left and **1a**·DME. Disorder in the guests was omitted for clarity.

interior cross-section diameter of 6.5 × 4.3 Å and contain encapsulated, disordered DME (Figure 3B, right) in a host–guest ratio of 2:1. The tubes form along the crystallographic *b* axis and are held together via hydrogen bonds between the ureas (d(N···O) = 2.848(4) and 2.929(4) Å) and π-stacking between neighboring TPAs. Individual columns are held together with π–π and halogen–π stacking interactions forming a hexagonal array similar to that of **1**·DMSO.

To generate different host–guest complexes of host **1a**, crystals of **1a**·DME were activated and loaded with new guests via SC-SC transformations.[40] Crystals of **1a**·DME were activated by heating under vacuum at 90 °C for 2.5 h to remove the DME. Next, a series of host–guest complexes (Figure 4) was prepared by immersing the activated crystals in
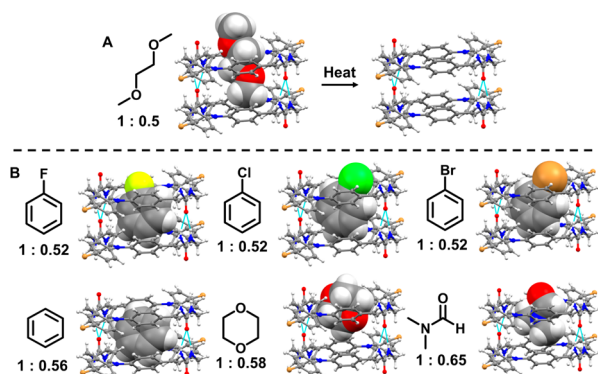
Figure 4. Guest inclusion complexes of **1a** with their host–guest ratios. (A) Heating of **1a**·DME results in an activated host. (B) Guests can then be added upon submersion of the activated crystals into a liquid of the new desired guest, resulting in an SC-SC transformation to afford a new host–guest complex. The DME complex, activated host, and four benzene derivative guest complexes have been previously reported,[40] while the DMF and 1,4-dioxane structures are new to these studies.

a guest solution for 24 h. Afterward, the crystals were filtered and air-dried affording the new host–guest complex. The activated host and benzene derivative loaded hosts of **1a** have been previously characterized via single-crystal X-ray diffraction (SC-XRD) and are all isoskeletal in regard to the macrocycle framework of **1**·DME. New to this work, DMF and 1,4-dioxane were also loaded into the nanotubes. Again, the host framework remained isoskeletal.

In the benzene derivative loaded complexes of **1a**, (Figure 4), the guests were arranged in a planar tapelike manner inside the channels and were modeled on two crystallographic independent sites.[40] These sites were located near inversion centers giving four possible sites for guest location. Each of these sites had similar occupancy giving an approximate host–guest ratio of 1:0.5. The 1,4-dioxane and DMF-loaded **1a** complexes exhibited a very similar guest disorder, although 1,4-dioxane was modeled on three independent crystallographic sites instead of two. Overall, the 1,4-dioxane and DMF guests exhibited host–guest ratios of 1:0.58(2) and 1:0.65(1), respectively. These loading ratios were higher compared to all the other modeled complexes, likely a result of the smaller size of these guests.

For comparison to the macrocycles, linear analogue **2** crystallized in the orthorhombic system in the centrosymmetric space group *Pbcn*. In this structure, both TPA groups extend to either side of a disordered methylene urea tether in a linear *trans-trans* arrangement (Figure 5). The disorder in the
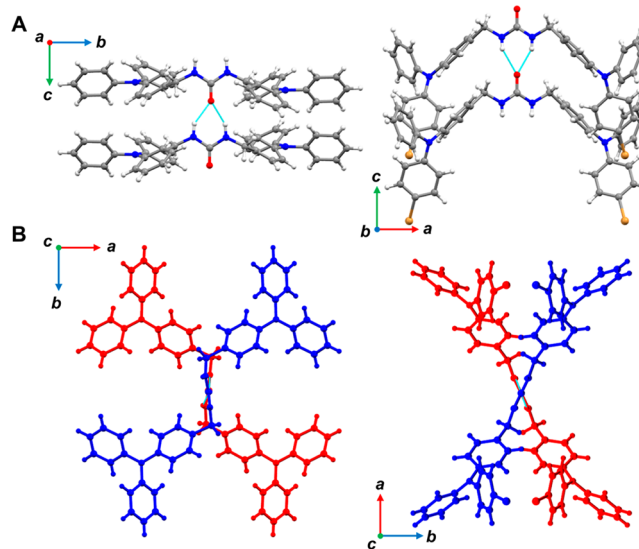
Figure 5. Comparison of triphenylamine linear analogues **2** (left) and **2a** (right). (A) Three-center urea hydrogen-bonding interactions stack the triphenyl amine groups on top of one another forming urea tape motifs. (B) Top-down view of the urea tapes showing either a cruciform pattern (left) or X-shaped pattern (right).

urea tether is oriented either up (50%) or down (50%) relative to the *c* axis, forming three-centered urea hydrogen-bonded chains (d(N···O) = 2.749(8) and 2.716(8) Å). The TPA groups, which are not disordered, organize in a cruciform pattern in relation to the urea chain with edge-to-face π-stacking from the TPAs holding alternating chains together (Figure S23).

The brominated derivative **2a** was similarly organized in the orthorhombic system in the *Pccn* space group.[39] TPA **2a** was also found in a linear *trans-trans* arrangement with both TPA groups extended out on either side of the methylene urea tether (Figure 5). The TPA units show minor disorder in this structure (5–9% depending on the chosen crystal) resulting from an opposite TPA rotation relative to the urea group. Overall, the urea groups still organize **2a** into chains along the crystallographic *c* axis (d(N···O) = 2.823(3) and 2.70(2) Å), resulting in an X-shaped pattern in projection along the chain direction instead of the cruciform pattern observed for TPA **2**.

Triphenylamines (**3** and **3a**) and urea derivative **4** were also crystallized. Together with the linear analogues and macrocycle **1**, this provides a series of control compounds for photophysical studies of macrocycle **1a**. The structure of TPA **3** has been previously reported (CCDC No. 1319035), and it crystallized in the monoclinic system in the *Bb* space group with multiple edge-to-face π-stacking interactions driving the assembly.[43] For TPA **3a**, two different polymorphs were found, crystallizing either as colorless needles (triclinic system, $P\bar{1}$ (No. 2) space group) or as colorless blocks (monoclinic system, $P2_1/c$ space group). The packing in both polymorphs was primarily driven through edge-to-face π-stacking interactions (Figures S24 and S25); however, the bromines stacked much closer to each other in the monoclinic polymorph (4.473 vs 6.230 Å). According to powder X-ray diffraction results, the bulk sample most similarly matched the monoclinic polymorph (Figure S30). Lastly, TPA **4** crystallized in the monoclinic space group $P2_1/c$ as colorless flakes. Assembly was organized through the three-centered urea hydrogen bond forming twisted chains along the crystallographic *c* axis similar to **2a** ($d(N\cdots O)$ = 3.069(3) and 3.028(2) Å) with additional stabilization coming via edge-to-face π stacking interactions (Figure S26).

To probe how structure, self-assembly, and guest encapsulation effects the photophysics of macrocycle **1a**, the absorption, emission, and photoluminescence lifetimes for solution and solid-state samples were measured. Table 1

Table 1. Measured Photophysical Properties for Compounds 1, 1a, 2, and 2a with Different Conditions

compound	λ_{abs}[a] (nm)	ε ($\times 10^4$ M^{-1} cm^{-1})	λ_{ems}[b] (nm)	τ_{avg}[c] (ns)
1	369, 414		478	1.6
10 μM **1a** in DMSO	303	4.65	378, 450*	2.3
1a	366		465	1.1
1a·DME	377		456	1.4
1a·C$_6$H$_6$	370		455	1.2
1a·DMF	372		456	1.3
2	366		487	1.5
10 μM **2a** in DMSO	302[d]	5.41[d]	369, 452*[d]	4.1[d]
2a	358[d]		447[d]	1.0[d]

[a]Peak position at largest absorption band. [b]Peak positions at largest emission bands in nanometers (largest denoted with * if applicable, excited at λ_{abs}). [c]Average lifetime of the most intense emission peak. [d]Values taken from ref 39.

compares the photophysics of macrocycle **1a** and linear analogue **2a** as 10 μM solutions in nitrogen-purged DMSO to the assembled crystals of **1**–**2a** and some guest inclusion complexes of host **1a**. In solution, macrocycle **1a** exhibits only one band in its absorption spectra with a λ_{max} at 303 nm and molar absorptivity of ~5 × 10^4 M^{-1} cm^{-1}, which is similar to its linear analogue counterpart **2a** under comparable conditions.[39] In the emission spectra, macrocycle **1a** shows two bands, with a smaller one at 378 nm and the larger one at 450 nm, also quite similar to linear analogue **2a**. The photoluminescence lifetime of macrocycle **1a** was quite short and approximately half of what was observed for linear analogue **2a** (2.3 vs 4.1 ns).

In the solid state, activated host **1a** showed a 60 nm red-shift of the absorption maxima versus dissolution in DMSO going from 303 to 366 nm (Figure S38). The formation of an

additional broad absorption band at ~400 nm was also observed. The shift in absorption is more typical for J-aggregation in planar dyes.[44] However, Yang et al. observed such shifts in crystalline styrene derivatized TPAs,[45] and we also observed a similar shift for the related linear analogue **2a**.[39] Similar absorption spectra were also observed for **1a**· DME, **1a**·C$_6$H$_6$, and **1a**·DMF. These host–guest complexes were chosen because of their polarity differences, since polarity played a large role in determining the photophysical properties of linear analogue **2a** in solution. Interestingly, the non-brominated TPAs of macrocycle **1** and linear analogue **2** also exhibited a red-shift in absorption, although their broad band at ~400 nm is comparatively more intense.

Assembly had less influence on the emission spectra and photoluminescent lifetimes for macrocycle **1a**. Indeed, activated host **1a** and its complexes (**1a**·DME, **1a**·C$_6$H$_6$, and **1a**·DMF) exhibited similar λ_{max} of emissions at ~460 nm upon excitation at the λ_{max} of absorption with similar lifetimes of ~1.2 ns. For comparison, activated **1**, **2**, and **2a**[39] show similar behavior with the nonhalogen-containing compounds exhibiting marginally longer lifetimes (1.5 ns) likely due to the lack of a heavy atom. Our hypothesis is that these shortened lifetimes are a result of nonradiative pathways, which may include radical formation.

Previously, we reported that UV irradiation of linear analogue **2a** generated radicals, which were unstable in solution resulting in degradation of the material.[39] Intriguingly, the radicals were found to be stable and persistent when generated within the assembled structures. Thus, we irradiated the activated host of **1a** to see if similar radicals would be observed. For this, freshly activated **1a** was sealed under argon and was examined by X-band EPR spectroscopy pre- and post-irradiation. For UV irradiation, 365 nm light-emitting diodes (LEDs) were employed instead of the medium pressure Hg lamp used previously.[38,39] The 365 nm LEDs are close to the λ_{max} of absorbance for these materials and show significant reduction in the background signal (see Supporting Information). Figure 6A compares the EPR signal of **1a** after 4 h of irradiation versus the pre-UV sample. After exhibiting very little signal pre-irradiation, the EPR signal exhibits a broad, axial powder pattern shape with a *g*-value of 2.008 post-irradiation.
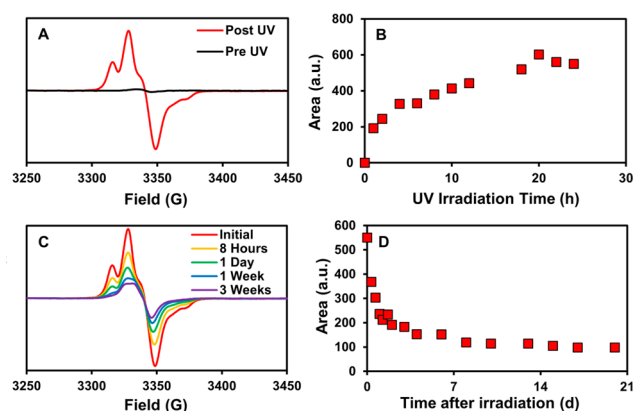
Figure 6. EPR studies for activated **1a**. (A) EPR signal pre- and post-UV irradiation. (B) Double integration over time of UV irradiation. (C) Dark decay spectra for activated **1a** after it was irradiated to its maximum radical concentration. (D) Double integration vs time after irradiation.

Next, we measured the EPR signal of activated **1a** (9.8 mg) under increasing irradiation time (1 to 24 h) to see if more radicals would be generated with longer irradiation times. To monitor the formation of radicals, we plotted the double integration of the EPR spectra over time. To estimate the number of radicals generated, the double integrations of the EPR spectra were compared to a calibration of Magic Blue standard solutions in dichloromethane (Figure S68). A comparison of these can give an approximate concentration of the number of radicals generated in the solid state. As seen in Figure 6D, the concentration of radicals grows with increasing irradiation time, until it plateaus at ~20 h. At this point, ~0.69% of the molecules generated a radical (or ~1 in 150 molecules), which estimates to the same number of radicals seen in 100 μL of a 0.83 mM solution of Magic Blue.

Next, seven host−guest complexes of **1a** were systematically investigated to quantify the maximum amount of radical they could generate upon irradiation. These complexes were chosen to vary the polarity and heavy atom substitution of the guests to see if they had any effects on radical formation. As seen in Figures S61−S67, most of these complexes reached their maximum EPR signals after ~20−24 h, apart from **1a**·C$_6$H$_5$F and **1a**·C$_6$H$_5$Cl, which reached a maximum after 12 h. Interestingly, the presence of encapsulated guests altered both the line shape of the signal as well as the quantity of radicals formed as seen in Figures 1 and 7 and Table 2,

Table 2. Approximate Number of Radicals Generated during UV Irradiation from 365 nm LEDs

compound	4 h	max
1	0.69%	
1a	0.42%	0.69%
1a·DME	0.20%	0.28%
1a·C$_6$H$_6$	0.55%[a]	0.85%[a]
1a·C$_6$H$_5$F	0.33%	0.45%
1a·C$_6$H$_5$Cl	0.19%	0.24%
1a·C$_6$H$_5$Br	0.13%	0.23%
1a·1,4-dioxane	0.24%	0.38%
1a·DMF	0.08%	0.15%
2	0.16%	
2a	0.16%	
3	~0%	
3a	very small[b]	
4	very small[b]	

[a]Average of four trials. A standard deviation of 0.06% was found for these trials. This is considered to be the error in all the measurements taken. [b]Concentration below values of calibration curve given in Figure S68.

Figure 7. EPR studies for guest inclusion complexes of **1a**. EPR signal pre and post UV irradiation is given for each complex. Additionally, the g-values are given.

respectively. This was quite surprising, since guest encapsulation had little effect on the absorption, emission, and lifetimes of host **1a**. For the line shapes, the least polar and least heavy atom substituted complex, **1a**·C$_6$H$_6$, showed the line shape most similar to the empty structure, activated **1a**, while the more polar, heavy atom complexes of **1a**·DMF and **1a**·C$_6$H$_5$Br showed a narrowing of the line shape. Similarly, the least polar and least heavy atom substituted complex, **1a**·C$_6$H$_6$, generated the most radicals (0.78%), while the more polar, heavy atom substituted complexes of **1a**·DMF and **1a**·C$_6$H$_5$Br exhibited the least number of radicals (0.15% and 0.23%, respectively). In fact, trends were observed along these lines with polarity (**1a**·C$_6$H$_6$ > **1a**·1,4-dioxane > **1a**·DME > **1a**·DMF) and heavy atom incorporation (**1a**·C$_6$H$_6$ > **1a**·C$_6$H$_5$F > **1a**·C$_6$H$_5$Cl > **1a**·C$_6$H$_5$Br) clearly affecting the amount of radical observed. Intriguingly, encapsulation of benzene within host **1a** afforded an even higher radical concentration than activated **1a**. This

may be due to a stabilization of the framework, or because the filled channel slows oxygen quenching processes.

To further estimate the error of these measurements, we repeated the **1a**·C$_6$H$_6$ experiment three more times, by irradiating the sample until radical formation plateaued (Figure S61). On average 0.85% of the molecules generated a radical at maximum concentration (or 1 in 120 molecules) with a standard deviation of 0.06%, which is considered to be the error on all the other measurements. Overall, this demonstrates the reproducibility of radical concentrations between samples.

Next, the persistence of the photogenerated radicals was examined with dark decay studies. For this, samples that were irradiated to their maximum concentration were stored in the dark at room temperature. Then EPR spectra were taken periodically afterward to assess the stabilities of the radicals. Figure 6C,D shows the EPR signal and the double integration of the EPR signal, respectively, over time for the activated **1a** host over three weeks. Figure 6D shows that the number of radicals decays to ~20% of the maximum concentration after one week, with an estimated half-life of ~24 h. The remaining radical species display more stability, with their concentration remaining somewhat constant up to three weeks later. These results, in combination with the different line shapes shown in the latter spectra (Figure 6C), suggest that at least two types of radical decay processes are occurring. Simulations of the EPR spectra (see below) also support this suggestion.

For the host−guest complexes, dark decay studies were performed on complexes **1a**·C$_6$H$_6$, **1a**·DME, and **1a**·DMF, as these guests afforded the greatest difference in radical concentrations (Table 2). Similar behavior and half-lives were observed for **1a**·C$_6$H$_6$ and **1a**·DMF crystals when compared to activated **1a** (Figures S61 and S63). A longer half-life of approximately one week was estimated for the **1a**·DME complex (Figure S62). Additionally, the radical concentration only dipped to ~40% of its maximum after three weeks instead of 20%, which was observed for all the other cases for host **1a**. This enhanced stability may be a result of minimal processing, as complex **1a**·DME is formed during the initial crystallization conditions for macrocycle **1a**. Activated **1a** is prepared by heating complex **1a**·DME to

remove the DME guest. Complexes $1a \cdot C_6H_6$ and $1a \cdot DMF$ are formed by soaking activated $1a$ crystals in neat C_6H_6 or DMF. The extra steps in crystal processing may explain why these three materials exhibit a shorter radical lifetime versus complex $1a \cdot DME$ during the dark decay of the radical signal. In fact, linear analogue $2a$, which also had minimal processing, displayed a similar half-life (one week), and decayed to only ~40% of its initial signal similar to complex $1a \cdot DME$.[39] Therefore, there is significant similarity between freshly crystallized samples. Overall, the line shapes of the EPR spectra for each case involving macrocycle $1a$ decayed to very similar signal levels, suggesting that the longer-lived radical species among these samples is similar.

Usually with chemical or electrochemical radical generation methods, the sample must be resynthesized once the TPA radicals have decayed due to degradation. However, no degradation was detected by NMR for linear analogue $2a$ after radical generation.[39] Moreover, after radical decay, re-exposure of linear analogue $2a$ to UV light led to regeneration of the radical species. This led us to test four samples of host $1a$ (activated $1a$, $1a \cdot DME$, $1a \cdot C_6H_6$, $1a \cdot DMF$) to determine if similar stable and regenerable radicals would be observed. For these experiments, each sample (5−10 mg) was irradiated to its maximum concentration, and its EPR spectrum was measured, followed by storage in the dark for 2 d. EPR signals were recorded at t = 8, 24, and 48 h. Then the samples were re-irradiated (12−14 h), so the cycle could be repeated. Figure 8
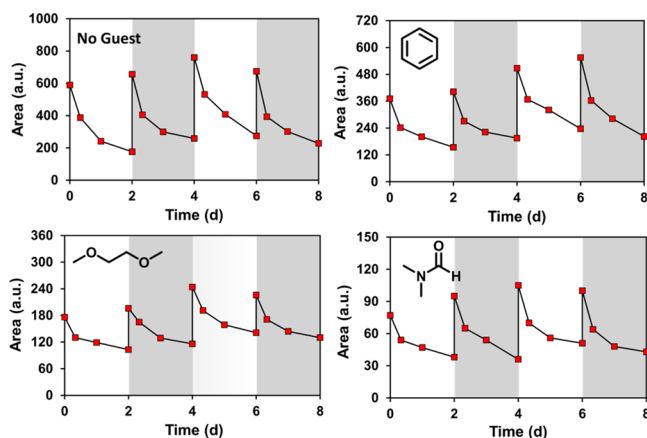
Figure 8. Regeneration of radical signals for activated $1a$, $1a \cdot C_6H_6$, $1a \cdot DME$, and $1a \cdot DMF$. After initial irradiation to maximum concentration, each sample was allowed to decay for 2 d. Then they were re-irradiated overnight to restore radical signal.

plots the area of the EPR signal versus time over four cycles of this photo-regeneration process for each sample. Remarkably, in all four cases, the radical signal could be fully restored in both intensity and line shape (Figures S60−S63). For complex $1a \cdot C_6H_6$, the maximum radical concentration slightly increased over each cycle. This unexpected result may be a consequence of some charge equilibria during radical decay, allowing for more charge to be introduced during later irradiation, since this is suspected to be a charge separation-based process.[39] Overall, in each case radicals could be formed, decay, and then formed again over multiple 2 d cycles, in a reproducible manner.

After seeing that the radicals could be repeatedly lost and regenerated, we wanted to monitor if the host material could survive this process similar to linear analogue $2a$.[39] For this,

each sample used from the regeneration studies (activated $1a$, $1a \cdot DME$, $1a \cdot C_6H_6$, $1a \cdot DMF$) was dissolved in DMSO-d_6, and the corresponding ^1H NMR spectra were recorded and compared to a freshly synthesized sample of $1a$. As seen in Figures S69−S72, no degradation was observed for any of the samples. Comparing these spectra, the only difference is the presence of guests in the NMR spectra (as is the case with benzene). These studies suggest that radical formation of host $1a$ is reversible and does not lead to the degradation of the material as a whole.

Next, we compared the EPR spectra for control compounds 1 and $2−4$ before and after irradiation (4 h, 365 nm LEDs) to investigate the chemical structure that contributes to radical formation (Figure 9 and Table 2). The first of these, TPA 3,
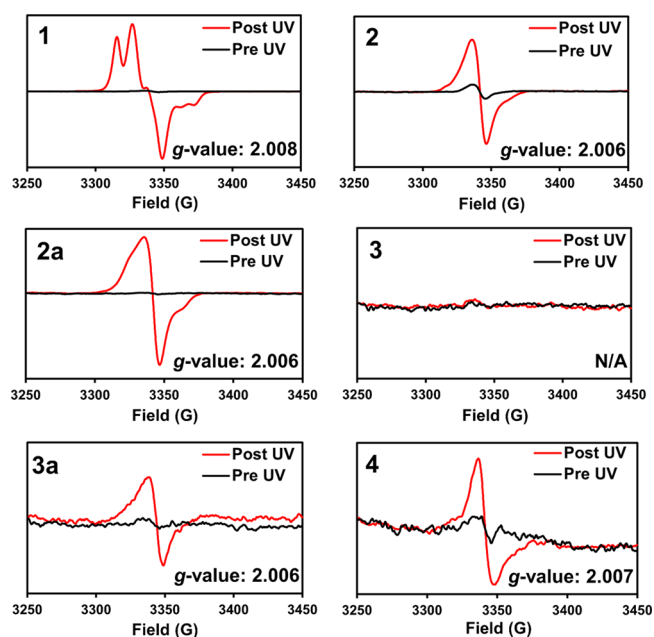
Figure 9. EPR signals pre- and post-irradiation for control samples 1, 2, $2a$, 3, $3a$, and 4. Each sample was irradiated for 4 h before the post-irradiation EPR spectrum was taken.

which has no substitution on the TPA group, displayed no significant radical formation after irradiation, suggesting that at least some substitution on the TPA moiety is needed for radical formation in the solid state. The monobrominated equivalent of TPA 3, compound $3a$, showed a very small signal after irradiation. This signal was so small that it was below the detection limits of our calibration curve to quantify the radical concentration. This suggests that the signal from TPA $3a$ does not arise from the same process as macrocycle $1a$, as many more radicals were produced for macrocycle $1a$. The radicals generated from TPA $3a$ may just be the result of photolysis of the C−Br bond, which can be expected for halogenated aromatics.[46] Control 4, which has one methylene urea connected to the TPA group, also exhibited a very small signal similar to the singly brominated TPA of $3a$, suggesting that it may also be susceptible to a small amount of photolysis.

Given these controls, we suspected that closely organizing two TPA units in a linear or macrocyclic system is important for generating significant radical concentrations in the solid state. Therefore, we tested the nonbrominated analogues of macrocycle $1a$ and linear analogue $2a$ to see if they afforded significant amounts of radical. Indeed, nonbrominated linear

analogue **2** forms a similar number of radicals as its brominated counterpart, **2a**, after 4 h of irradiation (both ∼0.16%). Surprisingly, the nonbrominated macrocycle **1** exhibited the highest efficiency of radical generation after 4 h of irradiation (0.69% for the nonbrominated macrocycle **1** vs 0.42% for the brominated macrocycle of **1a**) and showed more hyperfine interactions than its linear counterpart **2**. Considering that macrocycle **1a** also had more hyperfine splitting than its linear analogue counterpart **2a**, this suggests that the additional tether between the TPAs (macrocycles having two and linear analogues having one) increases the hyperfine splitting in the EPR spectra.

To investigate how UV-induced radical formation affected the TPA materials and to probe insight into a possible mechanism of radical formation, both linear analogue **2a** and the activated host of **1a** were further investigated by cross-polarized magic angle spinning (CP-MAS) ^{13}C NMR. Overlays of the NMR spectra of the pre- and post-irradiated solids are shown in Figure S73. While the methylene carbon resonances of the urea linker (ca. 43 ppm) were minimally affected, the overlays reveal significant UV-induced broadening of the aromatic and carbonyl ^{13}C lines, particularly for linear analogue **2a**. Thus, the proton spin–lattice relaxation times at different sites in crystals of the UV-irradiated linear analogue **2a** were probed by application of the inversion–recovery pulse sequence to the protons prior to cross-polarization and detection on ^{13}C (Figure S74). The longest ^{1}H spin relaxation times were observed for protons attached to the urea linker carbons, consistent with the minimal line broadening observed at these sites. In contrast, the T_1 relaxation times of the protons in the vicinity of the carbonyl carbon were among the shortest in the sample, where the recovery null occurs at ∼3.5 s. The proton T_1 of the protons on the aromatic rings varied and was shortest for broad resonance at ∼120 ppm and increased with increasing chemical deshielding, consistent with the observed variations in the line broadening. The ^{13}C CP-MAS NMR results suggest localization of unpaired electron density in the BrNPh$_3$ moiety. Significant line broadening on the carbonyl carbon but not the methylene carbon suggests radical formation impacts the urea network more strongly than the methylene bridge. To probe if the structure of the radicals changes with time, the stability of the UV-induced radicals were monitored over the course of 16 h by acquiring a series of ^{13}C CP-MAS spectra every 53 min. As seen in the overlay of these spectra in Figure S75, the spectra are all identical (within the noise), demonstrating the stability of the photoinduced radicals on the time scale of this experiment.

To gain more insight into structure of the photogenerated radicals we next investigated the more soluble TPAs **2**−**4** via electrochemical methods. Prior electrochemical studies with linear analogue **2a** demonstrated oxidation at 1.0 V versus a saturated calomel electrode (SCE) as a 1 mM solution in dichloromethane. This resulted in a dication with both TPA groups containing a radical cation.[39] Bulk electrolysis at this potential exhibited a very similar EPR spectrum to the photogenerated radicals of linear analogue **2a** in the solid state indicating that a similar radical species (radical cation) was present in both samples.

For this study, a cathodic investigation of TPA and its related derivatives were investigated with cyclic voltammetry. Voltammograms of TPAs **2**−**4**, Figures S76−S80, all exhibit irreversible reductions occurring between −1.2 and −1.5 V versus SCE as 1 mM dichloromethane solutions. Reduction of

TPA **3** occurred with an $E_{p,c}$ = −1.28 V under the standard experimental conditions. Reduction of the brominated TPA **3a** occurred at a less negative potential of $E_{p,c}$ = −1.18 V. This shift can be attributed to the electron-withdrawing Br moiety on TPA **3a**. In addition, reduction of methylene urea substituted TPA **4** occurred with a negative potential shift relative to TPA **3** likely due to the electron-donating behavior of the methylene urea substituent on the TPA core. These redox trends are consistent with previously reported redox behavior for related TPA derivatives.[47] Furthermore, linear analogues **2** and **2a** exhibit two closely spaced 1e$^-$ reductions. These reductions are attributed to reduction of the individual TPA units tethered by the urea linkers and illustrates an ability to generate closely spaced radicals.

Using the EPR, NMR, and electrochemical data, we next set out to simulate the EPR spectra of the UV-irradiated activated **1a**. Figure 10 shows our best effort to simulate the EPR
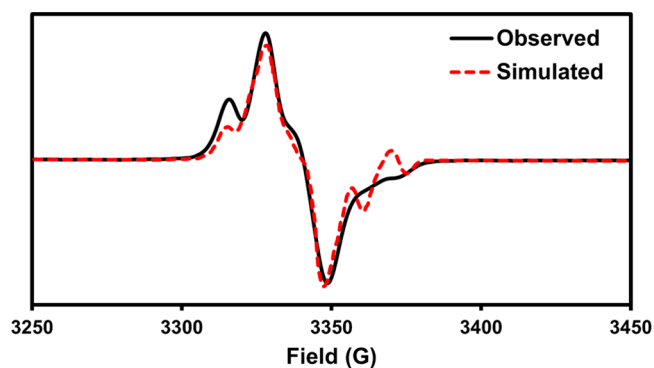
Figure 10. Experimental steady-state X-band EPR spectrum (solid black line) of activated host **1a** post-UV irradiation, overlaid onto a best-fit simulation (dashed red line) using EasySpin.[48] The simulation was performed using parameters for two independent radicals. The first has two nitrogen hyperfine interactions with g = 2.0049, a_N = 39 G for two equivalent nitrogens, line width (peak to peak) 5 G, and a relative weighting of 0.1. The second radical has g = 2.0087, contains no hyperfine interactions, line width = 20 G, and a relative weighting of 1.1.

spectrum with the most fine structure. The fact that two independent radicals are needed to get this reasonable fit, with all lines accounted for, supports that two radical decay processes may be at play. The discrepancies in intensity on the high-field side of the spectrum are almost certainly due to anisotropy in this solid-state spectrum. Furthermore, the presence of a signal carrier with two N hyperfine interactions and one without strongly supports the suggestion above that more than one redox pathway is available to these structures and that both monocations and dications may be present. Future isotopic substitutions and in situ electrochemical EPR experiments are planned to explore this further.

Overall, UV irradiation of self-assembled methylene urea tethered TPA macrocycles gives rise to persistent organic radicals. Guests loaded within the TPA hosts can modulate the concentration of radicals generated with concentrations ranging from 0.15 to 0.85% of the molecules generating a radical at maximum concentration. These radicals display a half-life of ∼24 h, persist an upward of three weeks, and can be regenerated with additional UV irradiation to their original maximum concentration without causing degradation to the TPA host. Future work with these TPA hosts could include

investigating how different electron-accepting guests affect the radical formation of the TPA host and if it leads to any new conductive properties of the material.

CONCLUSIONS

In summary, several TPA derivatives were synthesized and were organized in the solid state via crystalline assemblies. One of these derivatives, brominated macrocycle **1a**, organizes into robust columnar needles and displays one-dimensional (1D) porosity through small nanochannels. Inside these channels, small guests can be exchanged via SC-SC transformations without changing the host framework. This creates a series of isoskeletal complexes whose properties can be directly compared. We have monitored how the photophysics and photoinduced radical formation change with the inclusion of different guest molecules.

Although the absorption, emission, and photoluminescent lifetime properties of each complex were somewhat similar, the amount of photogenerated radicals produced by each complex varied considerably. It was found that an increase in polarity or heavy atom substitution decreases the number of radicals observed. This is highlighted in the complexes of $1a \cdot C_6H_6$, $1a \cdot$ DMF, and $1a \cdot C_6H_5Br$, with the first of these displaying the most radical formation after 24 h of irradiation with 0.78% of the molecules generating a radical. The latter two complexes are more polar or contain heavy atoms and show less radical formation after a similar amount of UV irradiation, 0.15% and 0.23%, respectively. The increase in radical formation by supramolecular encapsulation of less polar guests was surprising and differs from what is predicted in covalent radical systems that are substituted with both electron-donating and electron-withdrawing groups.[49,50] In such push—pull radicals, the captodative effect predicts that the radicals are more stable in polar solvents.[51] However, such effects appear to vary depending on the structure of the radicals. For example, alkoxy cyanomethyl radicals and cyclohexadienyl radicals showed no solvent effect.[52,53] Our observations, coupled with the persistent and regenerable nature of radicals in self-assembled TPA materials, will help guide the development of new photoactive materials in which the properties can be tuned simply via guest exchange. Thus, future work will focus on the mechanism of how the encapsulated guest and framework affects radical formation and lifetime.

Overall, the complexes reported here show similar radical half-lives of 24 h and persist up to three weeks. Intriguingly, re-irradiation of these materials with more UV light can regenerate radical quantities to similar amounts to their preradical decays. In fact, this radical formation/decay process can continue over several cycles with reproducible results and occurs without degradation of the host material. The key to forming these robust materials with regenerative radical properties is connecting two TPAs together through a methylene urea bridge. Although UV irradiation of simple bromine or methylene urea-substituted TPAs resulted in a small amount of radical signal, significant amounts of photogenerated radicals were not observed, until the two TPAs were connected. Currently, we are planning Q-band EPR, ENDOR, ESEEM, and SQUID experiments to try and pinpoint the mechanism of radical formation upon UV irradiation for these materials.

ASSOCIATED CONTENT

Ⓢ Supporting Information

The Supporting Information is available free of charge at https://pubs.acs.org/doi/10.1021/jacs.9b11518.

> Synthetic procedures, product characterization, X-ray, photophysical characterization, NMR, EPR, and cyclic voltammetry spectra (PDF)
> X-ray data for dibromide **1** (CIF)
> X-ray data for protected $1 \cdot CHCl_3$ (CIF)
> X-ray data for protected $1 \cdot MeOH$ (CIF)
> X-ray data for $1 \cdot DMSO$ (CIF)
> X-ray data for $1a \cdot DMF$ (CIF)
> X-ray data for $1a \cdot 1,4$-dioxane (CIF)
> X-ray data for **2** (CIF)
> X-ray data for monoclinic **3a** (CIF)
> X-ray data for triclinic **3a** (CIF)
> X-ray data for **4** (CIF)

AUTHOR INFORMATION

Corresponding Author

*shimizls@mailbox.sc.edu

ORCID Ⓞ

Baillie A. DeHaven: 0000-0003-2135-0029
Anil K. Mehta: 0000-0002-9867-151X
Malcolm D. E. Forbes: 0000-0003-4040-386X
Clifford R. Bowers: 0000-0001-6155-5163
Aaron K. Vannucci: 0000-0003-0401-7208
Linda S. Shimizu: 0000-0001-5599-4960

Present Address

⊥Department of Chemistry, Northwestern University, Evanston, Illinois 60208, United States.

Notes

The authors declare no competing financial interest.

ACKNOWLEDGMENTS

REFERENCES

(1) Mattia, E.; Otto, S. Supramolecular Systems Chemistry. *Nat. Nanotechnol.* **2015**, *10*, 111−119.
(2) Mahadevi, A. S.; Sastry, G. N. Cooperativity in Noncovalent Interactions. *Chem. Rev.* **2016**, *116*, 2775−2825.
(3) Steed, J. W. 21st Century Developments in the Understanding and Control of Molecular Solids. *Chem. Commun.* **2018**, *54*, 13175−13182.
(4) Ogoshi, T.; Kakuta, T.; Yamagishi, T. Applications of Pillar[*n*]arene-Based Supramolecular Assemblies. *Angew. Chem., Int. Ed.* **2019**, *58*, 2197−2206.
(5) Würthner, F.; Saha-Möller, C. R.; Fimmel, B.; Ogi, S.; Leowanawat, P.; Schmidt, D. Perylene Bisimide Dye Assemblies as Archetype Functional Supramolecular Materials. *Chem. Rev.* **2016**, *116*, 962−1052.
(6) Mills, M. B.; Wohlhauser, T.; Stein, B.; Verduyn, W. R.; Song, E.; Dechambenoit, P.; Rouzières, M.; Clérac, R.; Preuss, K. E. Magnetic Bistability in Crystalline Organic Radicals: The Interplay of H-Bonding, Pancake Bonding, and Electrostatics in 4-(2′-Benzimida-

zolyl)-1,2,3,5-dithiadiazolyl. *J. Am. Chem. Soc.* **2018**, *140*, 16904−16908.

(7) Liu, M.; Zhang, L.; Wang, T. Supramolecular Chirality in Self-Assembled Systems. *Chem. Rev.* **2015**, *115*, 7304−7397.

(8) Das, S.; Heasman, P.; Ben, T.; Qiu, S. Porous Organic Materials: Strategic Design and Structure-Function Correlation. *Chem. Rev.* **2017**, *117*, 1515−1563.

(9) Lin, R.-B.; He, Y.; Li, P.; Wang, H.; Zhou, W.; Chen, B. Multifunctional Porous Hydrogen-Bonded Organic Framework Materials. *Chem. Soc. Rev.* **2019**, *48*, 1362−1389.

(10) Dhakshinamoorthy, A.; Alvaro, M.; Garcia, H. Commercial Metal-Organic Frameworks as Heterogeneous Catalysis. *Chem. Commun.* **2012**, *48*, 11275−11288.

(11) Tan, Y.-X.; He, Y.-P.; Yuan, D.; Zhang, J. Use of Aligned Triphenylamine-Based Radicals in a Porous Framework for Promoting Photocatalysis. *Appl. Catal., B* **2018**, *221*, 664−669.

(12) Lü, J.; Cao, R. Porous Organic Molecular Frameworks with Extrinsic Porosity: A Platform for Carbon Storage and Separation. *Angew. Chem., Int. Ed.* **2016**, *55*, 9474−9480.

(13) Kitagawa, S.; Kitaura, R.; Noro, S. Functional Porous Coordination Polymers. *Angew. Chem., Int. Ed.* **2004**, *43*, 2334−2375.

(14) Tabacchi, G. Supramolecular Organization in Confined Spaces. *ChemPhysChem* **2018**, *19*, 1249−1297.

(15) Sumida, K.; Rogow, D. L.; Mason, J. A.; McDonald, T. M.; Bloch, E. D.; Herm, Z. R.; Bae, T.-H.; Long, J. R. Carbon Dioxide Capture in Metal-Organic Frameworks. *Chem. Rev.* **2012**, *112*, 724−781.

(16) Li, J.-R.; Sculley, J.; Zhou, H.-C. Metal-Organic Frameworks for Separations. *Chem. Rev.* **2012**, *112*, 869−932.

(17) Kreno, L. E.; Leong, K.; Farha, O. K.; Allendorf, M.; Van Duyne, R. P.; Hupp, J. T. Metal-Organic Framework Materials as Chemical Sensors. *Chem. Rev.* **2012**, *112*, 1105−1125.

(18) Wales, D. J.; Grand, J.; Ting, V. P.; Burke, R. D.; Edler, K. J.; Bowen, C. R.; Mintova, S.; Burrows, A. D. Gas Sensing Using Porous Materials for Automotive Applications. *Chem. Soc. Rev.* **2015**, *44*, 4290−4321.

(19) Comotti, A.; Bracco, S.; Sozzani, P. Molecular Rotors Built in Porous Materials. *Acc. Chem. Res.* **2016**, *49*, 1701−1710.

(20) Alhamami, M.; Doan, H.; Cheng, C.-H. A Review on Breathing Behaviors of Metal-Organic-Frameworks (MOFs) for Gas Adsorption. *Materials* **2014**, *7*, 3198−3250.

(21) Yanai, N.; Uemura, T.; Inoue, M.; Matsuda, R.; Fukushima, T.; Tsujimoto, M.; Isoda, S.; Kitagawa, S. Guest-to-Host Transmission of Structural Changes for Stimuli-Responsive Adsorption Property. *J. Am. Chem. Soc.* **2012**, *134*, 4501−4504.

(22) Akakuru, O. U.; Iqbal, M. Z.; Saeed, M.; Liu, C.; Paunesku, T.; Woloschak, G.; Hosmane, N. S.; Wu, A. The Transition from Metal-Based to Metal-Free Contrast Agents for T_1 Magnetic Resonance Imaging Enhancement. *Bioconjugate Chem.* **2019**, *30*, 2264−2286.

(23) Ratera, I.; Veciana, J. Playing with Organic Radicals as Building Blocks for Functional Molecular Materials. *Chem. Soc. Rev.* **2012**, *41*, 303−309.

(24) Forrester, A. R.; Hay, J. M.; Thompson, R. H. *Organic Chemistry of Stable Free Radicals;* Academic Press: New York, 1968.

(25) Ito, A.; Ino, H.; Tanaka, K.; Kanemoto, K.; Kato, T. Facile Synthesis, Crystal Structures, and High-Spin Cationic States of All-*para*-Brominated Oligo(*N*-phenyl-*m*-aniline)s. *J. Org. Chem.* **2002**, *67*, 491−498.

(26) Yano, M.; Sato, K.; Shiomi, D.; Ichimura, A.; Abe, K.; Takui, T.; Itoh, K. Synthesis of 1,3-Bis(diarylamino)benzenes as Model Precursors for One-Dimensional Organic Ferromagnetic Metals; Characterization of the Dications by Cyclic Voltammetry and Electron Spin Transient Nutation Spectroscopy. *Tetrahedron Lett.* **1996**, *37*, 9207−9210.

(27) Fukui, N.; Cha, W.; Shimizu, D.; Oh, J.; Furukawa, K.; Yorimitsu, H.; Kim, D.; Osuka, A. Highly Planar Diarylamine-Fused Porphyrins and their Remarkably Stable Radical Cations. *Chem. Sci.* **2017**, *8*, 189−199.

(28) Bill, N. L.; Ishida, M.; Bähring, S.; Lim, J. M.; Lee, S.; Davis, C. M.; Lynch, V. M.; Nielsen, K. A.; Jeppesen, J. O.; Ohkubo, K.; Fukuzumi, S.; Kim, D.; Sessler, J. L. Porphyrins Fused with Strongly Electron-Donating 1,3-Dithiol-2-ylidene Moieties: Redox Control by Metal Cation Complexation and Anion Binding. *J. Am. Chem. Soc.* **2013**, *135*, 10852−10862.

(29) Murata, H.; Miyajima, D.; Nishide, H. A High-Spin and Helical Organic Polymer: Poly{[4-(dianisylaminium)phenyl]acetylene}. *Macromolecules* **2006**, *39*, 6331−6335.

(30) Skorka, L.; Kurzep, P.; Chauviré, T.; Dubois, L.; Mouesca, J.-M.; Maurel, V.; Kulszewicz-Bajer, I. High-Spin Polymers: Ferromagnetic Coupling of $S = 1$ Hexaazacyclophane Units up to a Pure $S = 2$ Polycyclophane. *J. Phys. Chem. B* **2017**, *121*, 4293−4298.

(31) Su, C.; He, H.; Xu, L.; Zhao, K.; Zheng, C.; Zhang, C. A Mesoporous Conjugated Polymer Based on a High Free Radical Density Polytriphenylamine Derivative: Its Preparation and Electrochemical Performance as a Cathode Material for Li-Ion Batteries. *J. Mater. Chem. A* **2017**, *5*, 2701−2709.

(32) Chen, Z.; Su, C.; Zhu, X.; Xu, R.; Xu, L.; Zhang, C. Micro-/Mesoporous Conjugated Polymer Based on Star-Shaped Triazine Functional Triphenylamine Framework as the Performance-Improved Cathode of Li-Organic Battery. *J. Polym. Sci., Part A: Polym. Chem.* **2018**, *56*, 2574−2583.

(33) Agarwala, P.; Kabra, D. A Review on Triphenylamine (TPA) Based Organic Hole Transport Materials (HTMs) for Dye Sensitized Solar Cells (DSSCs) and Perovskite Solar Cells (PSCs): Evolution and Molecular Engineering. *J. Mater. Chem. A* **2017**, *5*, 1348−1373.

(34) Quinton, C.; Alain-Rizzo, V.; Dumas-Verdes, C.; Miomandre, F.; Clavier, G.; Audebert, P. Redox-Controlled Fluorescence Modulation (Electrofluorochromism) in Triphenylamine Derivatives. *RSC Adv.* **2014**, *4*, 34332−34342.

(35) Saha, A.; Chen, M.; Lederer, M.; Kahnt, A.; Lu, X.; Guldi, D. M. Sulfur Rich Electron Donors − Formation of Singlet *Versus* Triplet Radical Ion Pair States Featuring Different Lifetimes in the Same Conjugate. *Chem. Sci.* **2017**, *8*, 1360−1368.

(36) Moulin, E.; Armao, J. J.; Giuseppone, N. Triarylamine-Based Supramolecular Polymers: Structures, Dynamics, and Functions. *Acc. Chem. Res.* **2019**, *52*, 975−983.

(37) Shimizu, L. S.; Salpage, S. R.; Korous, A. A. Functional Materials from Self-Assembled Bis-urea Macrocycles. *Acc. Chem. Res.* **2014**, *47*, 2116−2127.

(38) DeHaven, B. A.; Goodlett, D. W.; Sindt, A. J.; Noll, N.; De Vetta, M.; Smith, M. D.; Martin, C. R.; González, L.; Shimizu, L. S. Enhancing the Stability of Photogenerated Benzophenone Triplet Radical Pairs through Supramolecular Assembly. *J. Am. Chem. Soc.* **2018**, *140*, 13064−13070.

(39) Sindt, A. J.; DeHaven, B. A.; McEachern, D. F.; Dissanayake, D. M. M. M.; Smith, M. D.; Vannucci, A. K.; Shimizu, L. S. UV-irradiation of self-assembled triphenylamines affords persistent and regenerable radicals. *Chem. Sci.* **2019**, *10*, 2670−2677.

(40) Sindt, A. J.; Smith, M. D.; Berens, S.; Vasenkov, S.; Bowers, C. R.; Shimizu, L. S. Single-crystal-to-single-crystal guest exchange in columnar assembled brominated triphenylamine bis-urea macrocycles. *Chem. Commun.* **2019**, *55*, 5619−5622.

(41) Ji, L.; Yuan, M.-S.; Liu, Z.-Q.; Shen, Y.-X.; Chen, H.-F.; Fang, Q. Switching high two-photon efficiency: from 3,8,13-substituted triindole derivatives to their 2,7,12-isomers. *Org. Lett.* **2010**, *12*, 5192−5195.

(42) Xu, D.; Ciszewski, L.; Li, T.; Repič, O.; Blacklock, T. J. Reductive alkylation of urea: a practical route to substituted ureas. *Tetrahedron Lett.* **1998**, *39*, 1107−1110.

(43) Sobolev, A. N.; Belsky, V. K.; Romm, I. P.; Chernikova, N. Y.; Guryanova, E. N. Structural Investigation of Triaryl Derivatives of the Group V Elements. IX.* Structure of Triphenylamine, $C_{18}H_{15}N$. *Acta Crystallogr., Sect. C: Cryst. Struct. Commun.* **1985**, *41*, 967−971.

(44) Würthner, F. Perylene Bisimide Dyes as versatile Building Blocks for Functional Supramolecular Architectures. *Chem. Commun.* **2004**, 1564−1579.

(45) Yang, M.; Xu, D.; Xi, W.; Wang, L.; Zheng, J.; Huang, J.; Zhang, J.; Zhou, H.; Wu, J.; Tian, Y. Aggregation-Induced Fluorescence Behavior of Triphenylamine-Based Schiff Bases: The Combined Effect of Multiple Forces. *J. Org. Chem.* **2013**, *78*, 10344−10359.

(46) Matsuura, T.; Omura, K. Photo-induced Reaction. III. The Synthesis of Biphenyls from Aromatic Bromo-Compounds. *Bull. Chem. Soc. Jpn.* **1966**, *39*, 944−947.

(47) Data, P.; Pander, P.; Zassowski, P.; Mimaite, V.; Karon, K.; Lapkowski, M.; Grazulevicius, J. V.; Slepski, P.; Darowicki, K. Electrochemically Induced Synthesis of Triphenylamine-based Polyhydrazones. *Electrochim. Acta* **2017**, *230*, 10−21.

(48) Stoll, S.; Schweiger, A. EasySpin a Comprehensive Software Package for Spectral Simulation and Analysis in EPR. *J. Magn. Reson.* **2006**, *178*, 42−55.

(49) Viehe, H. G.; Janousek, Z.; Mere'nyi, R. *Substituent Effects in Radical Chemistry*; Springer: Netherlands, 2012.

(50) Ito, O.; Matsuda, M. Solvent Effect on Rates of Free-Radical Reactions. 2. Addition of the *p*-(Dimethylamino)benzenethiyl Radical to α-Methylstyrene. *J. Phys. Chem.* **1984**, *88*, 1002−1005.

(51) Peterson, J. P.; Winter, A. H. Solvent Effects on the Stability and Delocalization of Aryl Dicyanomethyl Radicals: The Captodative Effect Revisited. *J. Am. Chem. Soc.* **2019**, *141*, 12901−12906.

(52) Beckhaus, H.-D.; Rüchardt, C. The Effect of Solvent on the Stability of mero-Substituted Alkyl Radicals. *Angew. Chem., Int. Ed. Engl.* **1987**, *26*, 770−771.

(53) Rhodes, C. J.; Roduner, E. Muon Spin Rotation Studies of the Role of Solvent in Captodative Interactions of Cyclohexadienyl Radicals. *Hyperfine Interact.* **1991**, *65*, 975−978.